atmosphere

MDPI

Article

Characteristics of DSD Bulk Parameters: Implication for Radar Rain Retrieval

Liang Liao [1,*], Robert Meneghini [2], Toshio Iguchi [3] and Ali Tokay [4]

1 Goddard Earth Science Technology & Research, Morgan State University, Baltimore, MD 21251, USA
2 NASA Goddard Space Flight Center, Greenbelt, MD 20771, USA; robert.meneghini-1@nasa.gov
3 Earth System Science Interdisciplinary Center, University of Maryland College Park, College Park, MD 20742, USA; toshio.iguchi@nasa.gov
4 Joint Center for Earth Systems Technology, University of Maryland Baltimore County, Baltimore, MD 21250, USA; ali.tokay-1@nasa.gov
* Correspondence: liang.liao-1@nasa.gov

Received: 30 April 2020; Accepted: 23 June 2020; Published: 25 June 2020

Abstract: With the use of 213,456 one-minute measured data of droplet-size distribution (DSD) of rain collected during several National Aeronautics and Space Administration (NASA)-sponsored field campaigns, the relationships between rainfall rate R, mass-weighted diameter D_m and normalized intercept parameter N_w of the gamma DSD are studied. It is found, based on the simulations of the gamma DSD model, that R, D_m and N_w are closely interrelated, and that the ratio of R to N_w is solely a function of D_m, independent of the shape factor μ of the gamma distribution. Furthermore, the model-produced ratio agrees well with those from the DSD data. When a power-law equation is applied to fit the model data, we have: $R = aN_wD_m^b$, where $a = 1.588 \times 10^{-4}$, $b = 4.706$. Analysis of two-parameter relationships such as R–D_m, N_w–R and N_w–D_m reveals that R and D_m are moderately correlated while N_w and D_m are negatively correlated. N_w and R, however, are uncorrelated. The gamma DSD model also reveals that variation of R–D_m relation is caused primarily by N_w. For the application of the Ku- and Ka-band dual-frequency radar for the retrieval of the DSD bulk parameters as well as the specific radar attenuations, the study is carried out to relate the dual-frequency radar reflectivity factors to the DSD and attenuation parameters.

Keywords: DSD; GPM DPR; disdrometer; rain retrieval; gamma distribution; dual-frequency radar

1. Introduction

Observations of rain-drop size distributions (DSD) have been carried out for more than seven decades evolving from early use of rather primitive tools to the deployment nowadays of sophisticated advanced disdrometers. The Autonomous Particle-Size-Velocity (PARSIVEL) Unit (APU) and Two-Dimensional Video Disdrometer (2DVD) are perhaps the most popular instruments that provide measurements of particle size spectra and velocities of falling hydrometeors. Knowledge of the DSD and its bulk or integral parameters is important not only in the understanding of precipitation microphysics and improvements in the microphysical parameterization in modeling studies [1] but also in development of active and passive satellite-based microwave sensor rainfall estimation [2–12].

Many studies indicate that the DSD varies not only with rain intensity but also with rain type, climate regime, and diurnal and seasonal changes [13–15]. To effectively account for the changes in the DSD, a three-parameter gamma model has widely been used to represent actual raindrop size spectra for radar retrieval of rain microphysical and bulk properties [16–20]. For instance, both the Tropical Rainfall Measuring Mission (TRMM) Precipitation Radar (PR) and the Global Precipitation Measurement (GPM) [21,22] Dual-frequency Precipitation Radar (DPR) algorithms have adopted the

gamma DSD model with a fixed shape factor (μ). This assumption enables the unknown parameter of the DSD to be expressed in terms of a normalized intercept parameter N_w and a mass-weighted diameter D_m. Although N_w and D_m are the characteristic parameters of the gamma DSD, they are the physical parameters that can be derived by integrating measured size spectra without use of the DSD parameterization model. Analysis of statistical characteristics of rainfall rate R, D_m and N_w obtained from the DSD measurement data are helpful to establish their interrelationships, which, in turn, serve as constraints in radar applications for rain and DSD estimation.

One of our objectives in this study is to use a large amount of the DSD measurements collected during the National Aeronautics and Space Administration (NASA)-sponsored field campaigns to explore how well R, D_m and N_w are statistically related. To check validity of the DSD parameterization and also to characterize the relationships between these bulk parameters, the gamma DSD model is incorporated into the measured DSD data. For the application of the Ku- and Ka-band dual-frequency radar for the retrieval of the DSD bulk parameters as well as the specific radar attenuations, the study will be extended to techniques for the estimation of these parameters by linking them to the dual-frequency radar reflectivity factors, specifically in terms of the Ku-band radar reflectivity and differential frequency ratio, which is defined as the difference of radar reflectivities between two frequencies. While our emphasis is on the utility of the dual-frequency technique, the uncertainties associated with the double solutions of the retrieval for light-to-moderate rain will also be analyzed.

This paper is organized as follows. A description of the DSD data as well as some basic equations to compute the DSD bulk parameters from the measured size spectra are provided in Section 2. In Section 3, formulation of the three-parameter gamma distribution in terms of N_w, D_m and μ is described, and the relationships between the bulk parameters of R, D_m and N_w are investigated, while the R–D_m, N_w–R and N_w–D_m relationships are explored in Section 4 by using both the DSD data and the model simulations. Estimations of the bulk parameters from the Ku- and Ka-band dual-frequency radar are prescribed in Section 5 followed by the summary in Section 6.

2. Droplet-Size Distribution (DSD) Measurement Data

The DSD spectra used in this study were measured by the PARSIVEL^2 disdrometers, and the data were collected during the Mid-latitude Continental Convective Clouds Experiment (MC3E) from 22 April–6 June 2011 near Lamont, Oklahoma, the Iowa Flood Studies (IFloodS) field experiment in eastern Iowa from 1 May to 15 June 2013, and the measurements from May 2013 to February 2014 at the NASA Wallops Flight Facility, located in Wallops Island, Virginia. The PARSIVEL disdrometers measure particle size spectra and fall-velocities of particle diameters from 0.3 to 20 mm with 32 size bins with higher resolutions for the sizes up to 10 mm and coarser spacing for sizes over 10 mm. Out of these measurements, 94,686, 80,104 and 38,675 1-min OTT PARSIVEL^2 data are selected from MC3E, IFloodS and Wallops, respectively, based on that the rain rates inferred from disdrometer data agree within 15% with those from co-located rain tipping bucket gauges. Quality control is also made to exclude non-rain precipitating hydrometeors. The particles are eliminated from rainy hydrometeors if their measured fall velocities exceed ±50% of the theoretical values. OTT PARSIVEL^2 is an upgrade version of PARSIVEL with its improvement documented by Tokay et al. [23]. The DSD measurements collected at 10 s intervals are averaged over one minute, and all rain events from a given disdrometer are merged into one file. By definition, D_m is computed from measured DSD, denoted by $N_m(D)$ in $mm^{-1}m^{-3}$, where D is the raindrop diameter in mm, by:

$$D_m = \frac{\int_{D_{min}}^{D_{max}} D^4 N_m(D) dD}{\int_{D_{min}}^{D_{max}} D^3 N_m(D) dD}, \quad (1)$$

where D_{min} and D_{max} are the minimum and maximum diameters, respectively. Similarly, rainfall rate (R) in mm/h is obtained by following equation:

$$R = 6\pi \times 10^{-4} \int_{D_{min}}^{D_{max}} N_m(D) D^3 V_m(D) dD, \quad (2)$$

where $V_m(D)$ in m/s is measured fall velocity of raindrop at a diameter of D.

As an example, Figure 1 shows a segment of DSD data versus time taken from one of the PARSIVEL disdrometers over 250 min. The image of $N_m(D)$ is given in the top panel with respect to D along the ordinate and time (minute) along the abscissa. R and D_m computed from $N_m(D)$ are given in the 2nd and 3rd panels, respectively, for the same time period. In addition, the normalized intercept parameter, N_w in $mm^{-1}m^{-3}$, of the DSD, when the DSD is parameterized as a gamma distribution, is also provided in the bottom panel. The definition of N_w will be detailed in Section 3. To illustrate frequency of occurrence in the data, Figure 2 provides the probability density functions (PDF) of R (top-left), liquid water content (LWC in g/cm^3) (top-right), D_m (bottom-left) and N_w (bottom-right) from the entire datasets collected from the disdrometers that have 213,465 one-minute DSD spectra in total. As clearly shown in Figure 2, the PDFs of logarithms of D_m and N_w closely follow the Gaussian distributions with their means of 1.13 mm and 7.57×10^3 $mm^{-1}m^{-3}$, respectively, while the PDFs of logarithms of R and LWC appear asymmetrical to their respective means of 2.12 mm/h and 0.11 g/m^3. Additionally, the standard deviations of R, LWC, D_m and N_w are 7.73 mm/h, 0.30 g/m^3, 0.58 mm and 1.52×10^4 $mm^{-1}m^{-3}$, respectively.

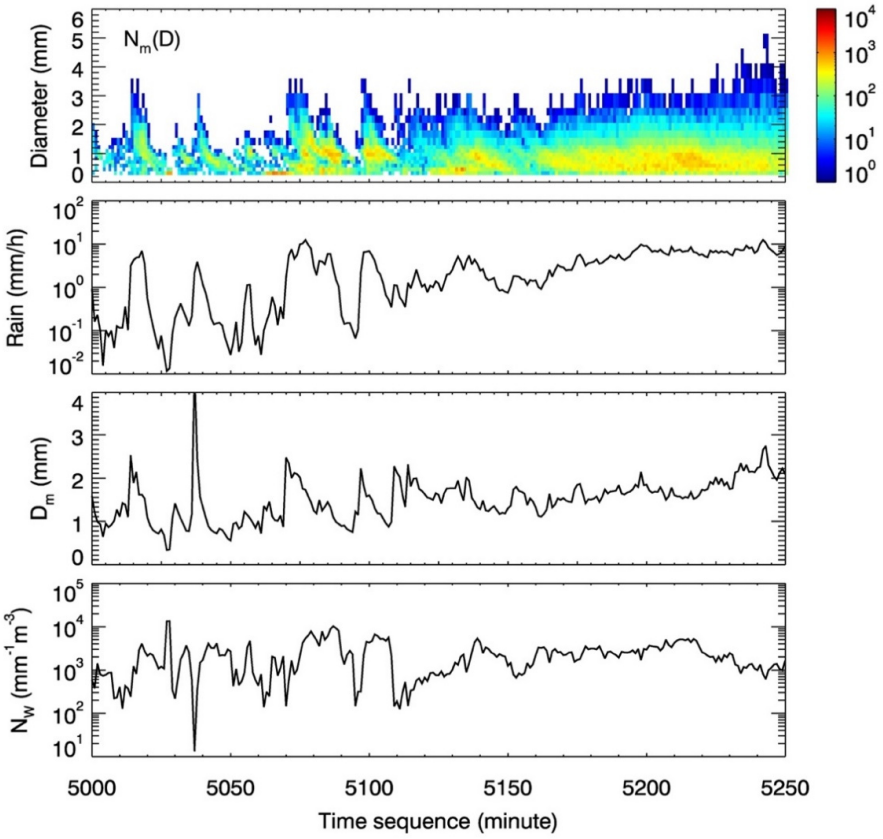

Figure 1. Example of the time-series droplet-size distribution (DSD) measurements from the time stamp 5000–5250, a total of 250 min. The size spectra are given in the top panel while rainfall rate R, mass-weighted diameter D_m and normalized intercept parameter N_w, which are derived directly from DSD, are provided in the 2nd, 3rd and 4th panels from the top, respectively.

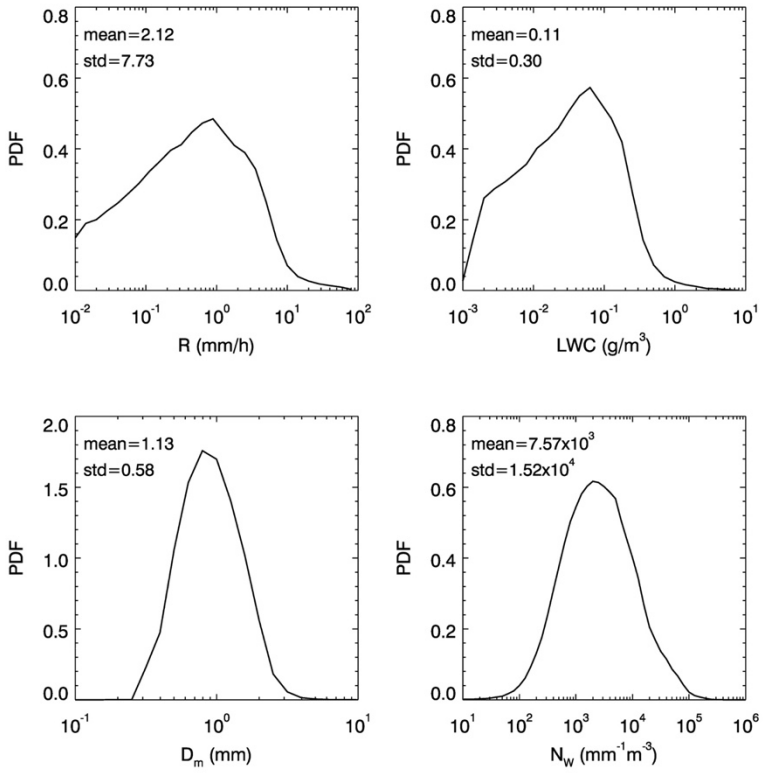

Figure 2. Probability density functions (PDF) of rainfall rate (R), liquid water content (LWC), D_m and N_w from 213,465 one-minute DSD data. The means and standard deviations (std) are also provided in the plot.

3. The Gamma DSD Model

The gamma distribution has been widely used to represent rain-drop size distribution N(D) ($mm^{-1}m^{-3}$) as a function of raindrop diameter D (mm). Its general form is given by:

$$N(D) = N_0 D^{\mu} \exp(-\Lambda D) , \quad (3)$$

where N_0 is the intercept parameter, μ is the shape factor, and Λ is the slope parameter expressed as:

$$\Lambda = \frac{(4+\mu)}{D_m}. \quad (4)$$

D_m is the mass-weighted mean diameter given by:

$$D_m = \frac{M_4}{M_3} , \quad (5)$$

where M_3 and M_4 are the 3rd and 4th moments of N(D), respectively. The ith moment of DSD is defined by:

$$M_i = \int_0^{\infty} D^i N(D) dD. \quad (6)$$

Substituting N(D) of Equation (6) with Equation (3) and using the gamma function, we obtain:

$$M_i = N_0 \frac{\Gamma(i+\mu+1)}{\Lambda^{i+\mu+1}} . \quad (7)$$

The liquid water content (LWC) in g/m^3 is:

$$\begin{aligned} \mathrm{LWC} &= \frac{\pi}{6} \times 10^{-3} \int_0^{\infty} \mathrm{N_0 D^{\mu}} \exp(-\Lambda \mathrm{D}) \cdot \mathrm{D^3 dD} \\ &= \frac{\pi}{6} \times 10^{-3} \mathrm{M_3} \\ &= \frac{\pi}{6} \times 10^{-3} \mathrm{N_0} \frac{\Gamma(4+\mu)}{\Lambda^{4+\mu}} . \end{aligned} \tag{8}$$

Note that water mass density with its value of 1 g/cm^3 is suppressed in Equation (8). From Equation (8), N_0 is:

$$\mathrm{N_0} = \frac{6}{\pi} \times 10^3 \mathrm{LWC} \frac{\Lambda^{4+\mu}}{\Gamma(4+\mu)} . \tag{9}$$

Inserting N_0 of Equation (9) into Equation (3) and then re-organizing it using Equation (4), we arrive at:

$$\mathrm{N(D)} = \left(\frac{4^4}{\pi} \times 10^3 \frac{\mathrm{LWC}}{\mathrm{D_m^4}} \right) \left(\frac{6(4+\mu)^{4+\mu}}{4^4 \Gamma(4+\mu)} \right) \left(\frac{\mathrm{D}}{\mathrm{D_m}} \right)^{\mu} \exp(-\Lambda \mathrm{D}). \tag{10}$$

Let

$$\mathrm{N_w} = \frac{4^4}{\pi} \times 10^3 \frac{\mathrm{LWC}}{\mathrm{D_m^4}} , \tag{11}$$

$$\mathrm{f(\mu)} = \frac{6(4+\mu)^{\mu+4}}{4^4 \Gamma(\mu+4)} , \tag{12}$$

Equation (10) becomes

$$\mathrm{N(D)} = \mathrm{N_w f(\mu)} \left(\frac{\mathrm{D}}{\mathrm{D_m}} \right)^{\mu} \exp(-\Lambda \mathrm{D}). \tag{13}$$

N_w is in units of mm^{-1}m^{-3}, and often called as the DSD normalized intercept parameter while f(μ) is unitless. The form of the gamma distribution expressed in Equation (13) is widely used in rain and snow precipitation retrieval [7,9,16–19,24]. From Equation (13), the rainfall rate is given by:

$$\mathrm{R} = 6\pi \times 10^{-4} \int_0^{\infty} \mathrm{N_w f(\mu)} \left(\frac{\mathrm{D}}{\mathrm{D_m}} \right)^{\mu} \exp(-\Lambda \mathrm{D}) \mathrm{D^3 V(D) dD}, \tag{14}$$

where V(D) is raindrop fall velocity (m/s) and is expressed as a function of the raindrop diameter proposed by Lhermitte [25]:

$$\mathrm{V(D)} = 9.25 \left[1 - \exp\left(-0.068 \mathrm{D^2} - 0.488 \mathrm{D} \right) \right]. \tag{15}$$

It is important to note that R, LWC, D_m and N_w are the bulk parameters that can be derived directly from DSD data without assuming a DSD model. Equation (11) yields an analytical relationship among the quantities LWC, D_m and N_w, from which it follows that from any two DSD bulk parameters LWC, D_m and N_w, the third is determined uniquely. To explore the possibility of a similar relationship among R, D_m and N_w, two approaches are investigated. One is based on the DSD-based regression from which a power-law fit is performed between the R/N_w and D_m data that are derived directly from the measured DSD. The second approach is to compute the same quantities from the DSD gamma model. Shown in Figure 3 are the DSD-based and model-based results, i.e., the ratios of R to N_w as a function of D_m. The model results are given by various line-style blue curves computed at μ values of 0, 3, 6 and 10 while the red filled-circles are those derived from the measured DSD (213,465 1-min DSD spectra). It is not difficult to find that the model results are nearly independent of μ as demonstrated by the fact that the curves are indistinguishable for different μ values. These results, however, almost perfectly coincide with those from the DSD measurements that show little variation in log-log space.

The power-law regression is applied to the gamma DSD model data for μ values assumed from 0 to 10. This gives:

$$R = aN_w D_m^b \tag{16}$$

where

$$a = 1.588 \times 10^{-4},\ b = 4.706$$

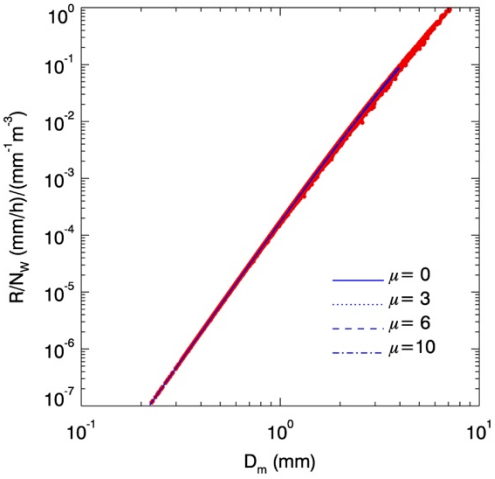

Figure 3. The ratios of R to N_w in terms of D_m, derived from the gamma DSD models with μ values varying from 0 to 10 (blue curves) and from the DSD measurement data (red dots).

From above equation, we have

$$D_m = \left(\frac{R}{aN_w}\right)^{\frac{1}{b}} \tag{17}$$

$$N_w = \frac{1}{a} R D_m^{-b} \tag{18}$$

To check the validity and accuracy of Equations (16)–(18), used to reproduce R, D_m and N_w, we employ the aforementioned DSD data and compare the estimates of R, D_m and N_w to the same quantities derived directly from the DSD data. For example, R, as estimated from (16) with inputs of the DSD-derived D_m and N_w, is compared against the value obtained directly from the corresponding measured DSD spectrum. For simplicity, the quantities obtained from the DSD data are referred to as truth or true values while those that are derived from Equations (16)–(18) are referred to as the estimates. Provided in Figure 4 are the scatter plots of the estimates of R (left), D_m (middle) and N_w (right) versus their respective true values. Not surprisingly, the comparisons made in Figure 4 reveal excellent agreement between the estimates and truth, evidenced by the fact that there are nearly perfect correlations (that round to 1.00) and small rms (root mean square) errors (0.99 mm/h in R and 0.03 mm in D_m) despite the rms error in N_w (926 $mm^{-1}m^{-3}$), which, however, is still fractionally small in view of its large dynamic range and mean value of 7.6×10^3 $mm^{-1}m^{-3}$. It is worth reiterating that the Equations (16)–(18) are based on the gamma DSD model with μ ranging from 0 to 10 rather than the measured DSD data, and are therefore independent of the measured DSD data that vary seasonally as well as geographically. Agreement between the estimates and their true values indicate that D_m and N_w can be used to characterize R with sufficient accuracy.

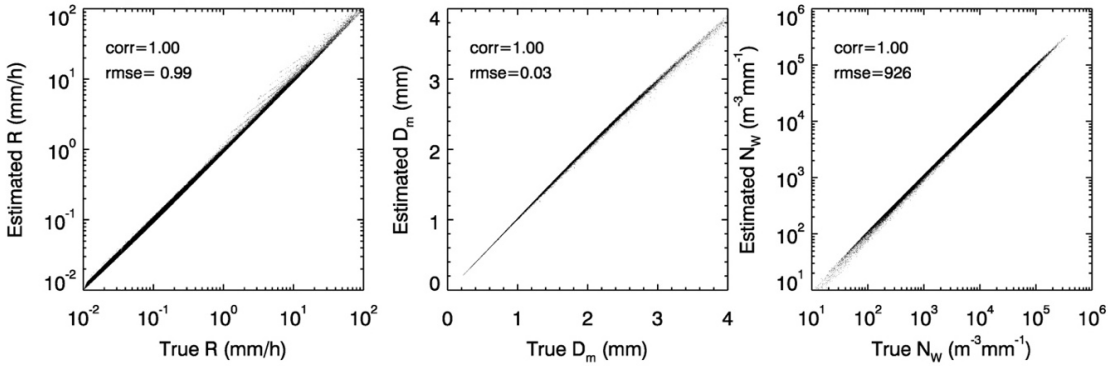

Figure 4. Scatter plots of the estimates in R (**left**), D_m (**middle**) and N_w (**right**) and their respective true values. Correlations between the estimates and truth and rms errors of the estimates, denoted by 'corr' and 'rmse', respectively, are also given.

4. Rainfall Rate–Mass-Weighted Diameter (R–D_m), Normalized Intercept Parameter (N_w)–R and N_w–D_m Relations

Figure 3 suggests that three variables of R, D_m and N_w are closely related, and their relations are given by Equations (16–18). However, in many situations of rain retrieval, the radar equations are often under constrained, which means that there are more unknown variables than the number of equations as a result of limited independent radar measurements. As such, the constraints among the DSD parameters as in Equations (16–18) need to be relaxed to some extent to make the retrieval solutions robust and achievable. One important example of this situation is the GPM DPR operational algorithm that takes on a nominal R–D_m relation along the radar profile and then applies an adjustable parameter ε to modify the R–D_m relation to minimize the cost function [9,26]. This cost function depends on several factors, one of which is minimizing the difference of independently measured path attenuations between Ku- and Ka-band. Other factors are the mean and standard deviation of the Gaussian distribution of ε as well as the rms difference between the simulated and measured Ka-band reflectivities. To exploit the R–D_m, N_w–R and N_w–D_m relationships and also explore their correlations, the DSD data are employed. Figure 5 illustrates the two-dimensional PDFs of N_w–R (Figure 5a), N_w–D_m (Figure 5b) and R–D_m (Figure 5c) as well as their corresponding scatter plots of N_w–R (Figure 5d), N_w–D_m (Figure 5e) and R–D_m (Figure 5f). The pixel colors of the bottom panel show the mean values of D_m (Figure 5d), logarithms of R (Figure 5e) and N_w (Figure 5f) in the planes of N_w–R, N_w–D_m and R–D_m, respectively. The theoretical model computations from the gamma DSD with a fixed μ of 3 are also superimposed on the plots. As shown in Figure 5, the correlation between N_w and R is −0.03, indicating that they are nearly uncorrelated. The correlations of N_w–D_m and R–D_m are −0.32 and 0.44, respectively. These results indicate that a large amount of uncertainty would occur in estimating R from N_w alone, but this uncertainty will be reduced if D_m is used instead. Also, there exists a certain degree of error in inferring N_w from D_m without knowing R. The colored scatter plots of Figure 5 in fact reveal how the two-parameter relations are a function of the third one. In the logarithmic scale of N_w and R the data points with constant D_m lie along ~45° straight lines and move toward the bottom-right direction as D_m increases. Likewise, the contours of R in N_w–D_m and N_w in R–D_m are straight lines and parallel to one another which are plotted in logarithmic scales. The image pattern that changes slowly with D_m and spans vast area along the direction perpendicular to constant D_m lines, as shown in the N_w–R plane (Figure 5d), reveals large variation in the N_w–R relation, indicating a strong dependence of the N_m–R relation on D_m. On the other hand, the relatively small variations shown in the images of N_w–D_m (Figure 5e) and R–D_m (Figure 5f) imply relatively weak dependencies of N_w–D_m on R and R–D_m on N_w.

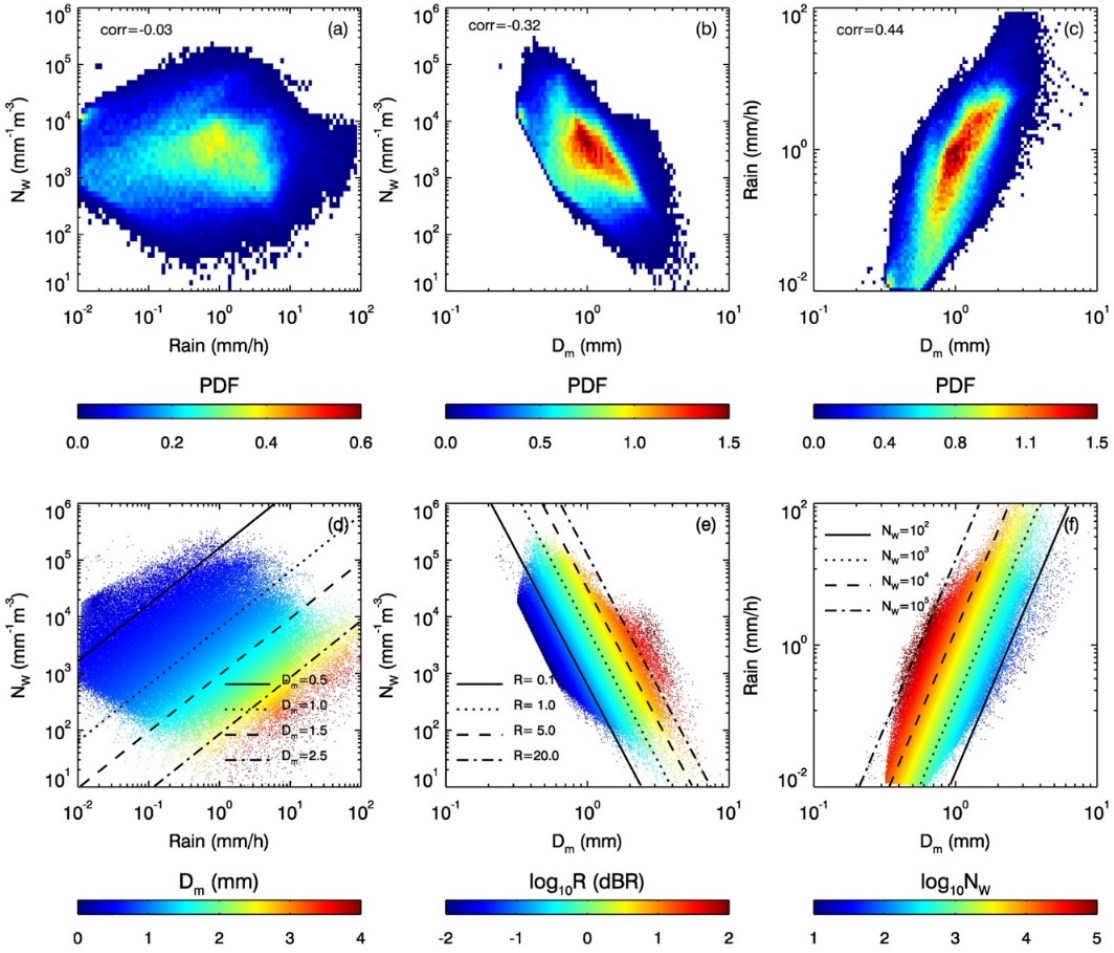

Figure 5. Two-dimensional PDFs of N_w–R (**a**), N_w vs. D_m (**b**) and R vs. D_m (**c**), and images of D_m in N_w–R plane (**d**), R in N_w–D_m plane (**e**) and N_w in R–D_m plane (**f**) with their respective color scales shown at the bottom of the plots, obtained from 213,465 1-min DSD data. Theoretical computational results based on the gamma DSD model with $\mu = 3$ (black lines) are superimposed on the bottom plots. The correlations between two parameters are provided in the top panel.

Figure 6 displays the power-law fittings of N_w–D_m (left) and R–D_m (right) to the data along with the DSD model results. The solid lines are the results that are statistically fitted to the data by using the method of least-squares, and the dotted lines are those with the exponents fixed at the values found in Equations (16) and (18), i.e., −4.706 for the N_w–D_m relation and 4.706 for the R–D_m relation, with which the scale factors are fitted to the data. The fitting curves using the DSD model-derived exponents are denoted by 'model' in the plots. For comparison, the DPR-default R–D_m relations are also provided, in which the notations of 'DPR-s' and 'DPR-c' represent the cases of stratiform and convective rain, respectively. The resultant fitting coefficients are summarized in Table 1. Because of large variations in the data between N_w and D_m as well as R and D_m, as reflected by their moderate correlations shown in Figure 5, the regressions to these data depend on the methods selected and physical models applied. The model-based regressions, though they differ from the data fittings, represent fairly well the N_w–D_m and R–D_m relations judging by their consistency with the PDFs. It is worth reiterating that R and N_w are constant along the model-based N_w–D_m and R–D_m fitting curves, respectively. The R–D_m relation based on the DSD model agrees better with the nominal R–D_m relations adopted by the DPR standard algorithm than the relation that is obtained by fitting directly to the data.

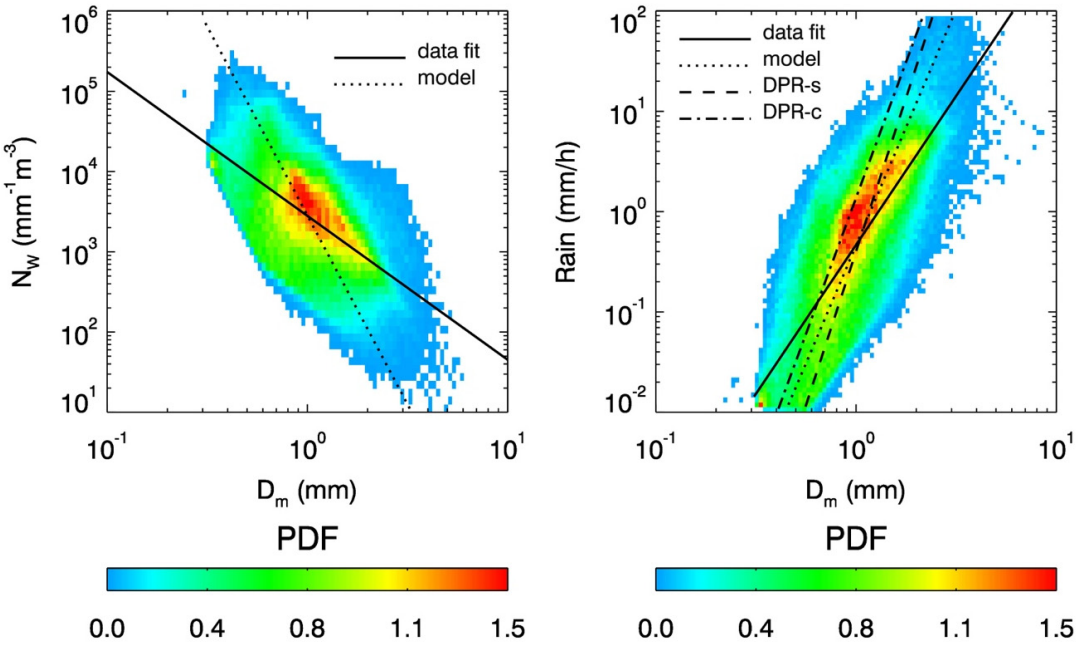

Figure 6. Power-law regressions of N_w–D_m (**left**) and R–D_m (**right**) relations obtained from the DSD data. Similar to top panel of Figure 5, the color graphs represent PDFs of the data.

Table 1. Coefficients of the power-law N_w–D_m and R–D_m relations derived from the DSD data and the DSD models as well as the R–D_m relations adopted by the DPR operational algorithm.

Method	$N_w = a_N D_m^{b_N}$		$R = a_R D_m^{b_R}$	
	a_N	b_N	a_R	b_R
Data Fitting	2807.59	−1.793	0.466	2.970
Model	2845.90	−4.706	0.464	4.706
DPR-s			0.401	6.131
DPR-c			1.370	5.420

5. DSD Bulk Parameters Linked to Ku- and Ka-band Radar Parameters

As discussed above, the DSD bulk parameters R, D_m and N_w are closely interrelated. These parameters are of importance for precipitation modelling and weather prediction studies. The relation between radar parameters and these DSD bulk parameters comprises a basis for radar rain retrieval. Although the purpose of our study is to explore applications to the Ku- and Ka-band dual-frequency radar, development of the full radar algorithm for the retrieval of rain profiles is beyond the goal of this paper. To establish the statistical characteristics of relationships between the DSD and dual-frequency radar parameters, such as Ku- and Ka-band radar reflectivity factors, the radar reflectivities are simulated by prescribing raindrops as oblate spheroids whose axis ratios yield the shape–size relations described by Thurai et al. [27]. The T-matrix method [28] is applied to obtain the scattering properties of single particles assuming a nadir-viewing radar and taking the major axes of raindrops to be in the horizontal plane. It should be noted that the raindrop diameter throughout the paper actually refers to an oblate drop with a volume-equivalent diameter D. Because of the fact that the Ku- and Ka-band radar signals are attenuated by raindrops while propagating through rain, attenuation corrections to the measured reflectivities are needed before the DSD retrieval. Specific attenuations (dB/km), denoted by k_{Ku} and k_{Ka} at Ku- and Ka-band, respectively, are the parameters that are used to account for the attenuation along the propagation path to the range gate at which the retrieval occurs. In addition to R, D_m and N_w, the estimates of k_{Ku} and k_{Ka} are crucial for development of radar profiling algorithms. Conventionally, the specific attenuation is fitted to measured DSD in terms of

reflectivity factor, such as k_{Ku}–Z_{Ku} and k_{Ka}–Z_{Ka} relations. These relations have been widely used for single-frequency radar retrieval [5,29,30]. However, k_{Ku} and k_{Ka} could be better estimated if both the Ku- and Ka-band reflectivities were used. In dual-frequency radar applications, one of the most important parameters is the dual-frequency ratio (DFR), which is defined as

$$\mathrm{DFR} = 10\log_{10}\left(\frac{Z_{Ku}}{Z_{Ka}}\right), \tag{19}$$

where Z_{Ku} and Z_{Ka} are the radar reflectivity factors at the Ku- and Ka-band, expressed by

$$Z_\lambda = \frac{\lambda^4}{\pi^5|K_w|^2}\int_0^\infty N(D)\sigma_b(D,\lambda)dD, \tag{20}$$

where λ is wavelength, referring to either Ku- or Ka-band, and $\sigma_b(D,\lambda)$ is the backscattering cross section of a particle with diameter of D. By convention, $|K_w|^2$ is taken to be 0.93 for liquid water. DFR has many applications ranging from snow and rain retrievals to hydrometeor phase identification [2,24,31,32].

For the gamma DSD model given in Equation (13), DFR is independent of the N_w, and therefore D_m is directly related to DFR for a given μ. Other parameters like R, N_w, k_{Ku} and k_{Ka}, however, are a function of not only DFR but also Z_{Ku} or Z_{Ka}. To link these parameters to the DFR and Z_{Ku}, the R, N_w, k_{Ku} and k_{Ka} are first normalized by Z_{Ku}, and then these normalized parameters are related to DFR. The top panel of Figure 7 provides the PDFs of the data obtained from the measured DSD in the planes of R/Z_{Ku}–DFR (Figure 7a), D_m–DFR (Figure 7b) and N_w/Z_{Ku}–DFR (Figure 7c). Similar plots are made in the bottom panel of Figure 7. Instead of the PDFs, the bin-averaged R on logarithmic scale in the R/Z_{Ku}–DFR (Figure 7d) and D_m–DFR (Figure 7e) planes as well as logarithmic N_w in the N_w/Z_{Ku}–DFR (Figure 7f) plane are plotted. The PDFs reveal two-dimensional distributions of occurrence frequencies of the data in the planes comprising DSD and radar parameters while the images of the lower panel reflect changes in R and N_w. For example, in the PDF of R/Z_{Ku} vs. DFR (Figure 7a) most of the DSD data are clustered in the region where DFR values are small, and the rain rates of these data increase with DFR as shown in the bottom-left image. The plots show that there exist two values of the normalized DSD parameters for a given DFR in the regions where DFR is less than 0, which typically correspond to light-to-moderate rain with averaged D_m less than 1 mm and N_w greater than 10^3 $mm^{-1}m^{-3}$. Beyond these regions, however, good correspondences are found between the DSD parameters of R, D_m and N_w and the radar parameters of Z_{Ku} and DFR. This actually offers a means to infer the DSD parameters from the radar measurements. In particular, R can be estimated by, first, deriving R/Z_{Ku} from DFR and then multiplying the result by Z_{Ku}. The same procedure can be applied to estimate N_w. D_m, on the other hand, is directly obtained from DFR. For reference, the computational results from the gamma DSD model with a fixed μ of 3 (black dashed lines) are also plotted in Figure 7. The gamma model appears to be a reasonably good approximation (dashed lines) from the perspective of the Ku- and Ka-band retrieval.

The issue of double solutions when DFR < 0 inevitably leads to large ambiguities in the DSD retrieval. The small, negative values of DFR are a consequence of the fact that the Ku- and Ka-band reflectivities are nearly identical for the case of light rain which is composed primarily of small raindrops. In these cases, Rayleigh scattering, where the backscattering cross section is proportional to the 6th power of particle diameter and independent of radar frequency, dominates at both frequencies. If the Ku- and Ka-band radar falls into the Rayleigh scattering regime, the 2nd frequency measurement basically doesn't provide additional information. It is worth noting that out of 213,465 1-min DSD spectra employed in this study, nearly half of them are either in the double-solution region or under the Rayleigh scattering. An attempt to mitigate the double-solution impact has recently been studied by Liao and Meneghini [12].

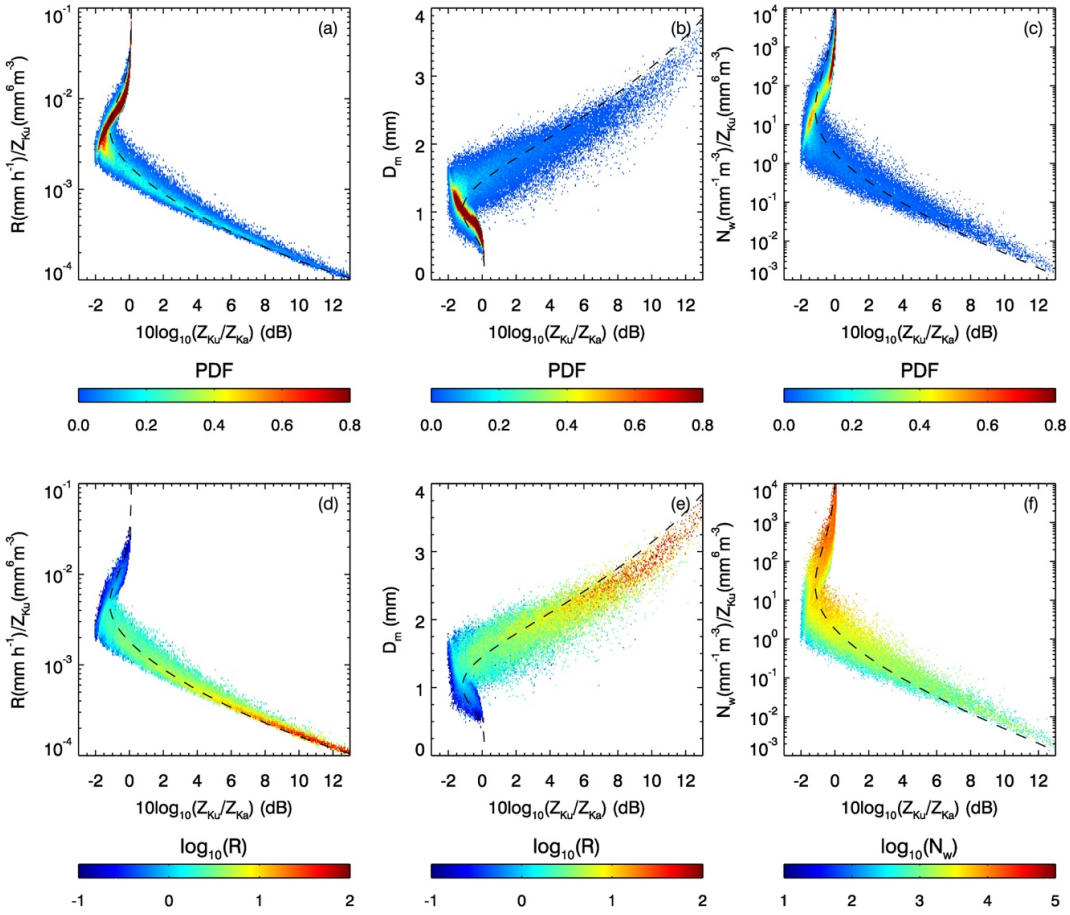

Figure 7. PDFs of the data obtained from the measured DSD in the planes of the R/Z_{Ku}–DFR (dual-frequency ratio) (**a**), D_m–DFR (**b**), and N_w/Z_{Ku}–DFR (**c**). Also shown are the images of the averaged R in the planes of the R/Z_{Ku}–DFR (**d**) and D_m–DFR (**e**) and the image of the -averaged N_w in the plane of the N_w/Z_{Ku}–DFR (**f**). The computational results from the gamma DSD model with $\mu = 3$ (black dashed lines) are provided.

Comparison of the gamma DSD results with those computed directly from the DSD data suggests that there is less uncertainty in the estimates of R than in the estimates of D_m and N_w for the region where DFR > 0 because of the fact that relatively small variability is found in R given a pair of DFR and Z_{Ku} values as compared with D_m and N_w. As mentioned earlier, the DSD model results shown in Figure 7 are from the gamma DSD with $\mu = 3$, which is the case for the GPM DPR operational algorithm [33]. The results from the gamma DSD with different μ are also computed (not shown), and reveal that there are only small changes in the estimates of R. This, however, is not the case for either D_m or N_w.

Similar to Figure 7, Figure 8 displays the PDFs (Figure 8a,b) of the Z_{Ku}-normalized specific attenuations versus DFR and the bin-averaged specific attenuations (Figure 8c,d) at Ku- (Figure 8a,d) and Ka-band (Figure 8b,d). The results shown in Figure 8 resemble many of the features found in Figure 6, i.e., there are the double-solution regions that are identical to those found in R, D_m and N_w. In the region when DFR > 0, k_{Ku} and k_{Ka} increase with an increase of DFR, and show relatively small spreads as seen in the PDF plots. Again, the fixed $\mu = 3$ gamma DSD results denoted by black dashed curves, show good approximations to those obtained from the DSD data. While the combination of Z_{Ku} and DFR leads to fairly good estimates of k_{Ku} and k_{Ka}, as in the estimates of R, D_m and N_w, the application to the double-value region still remains a challenge.

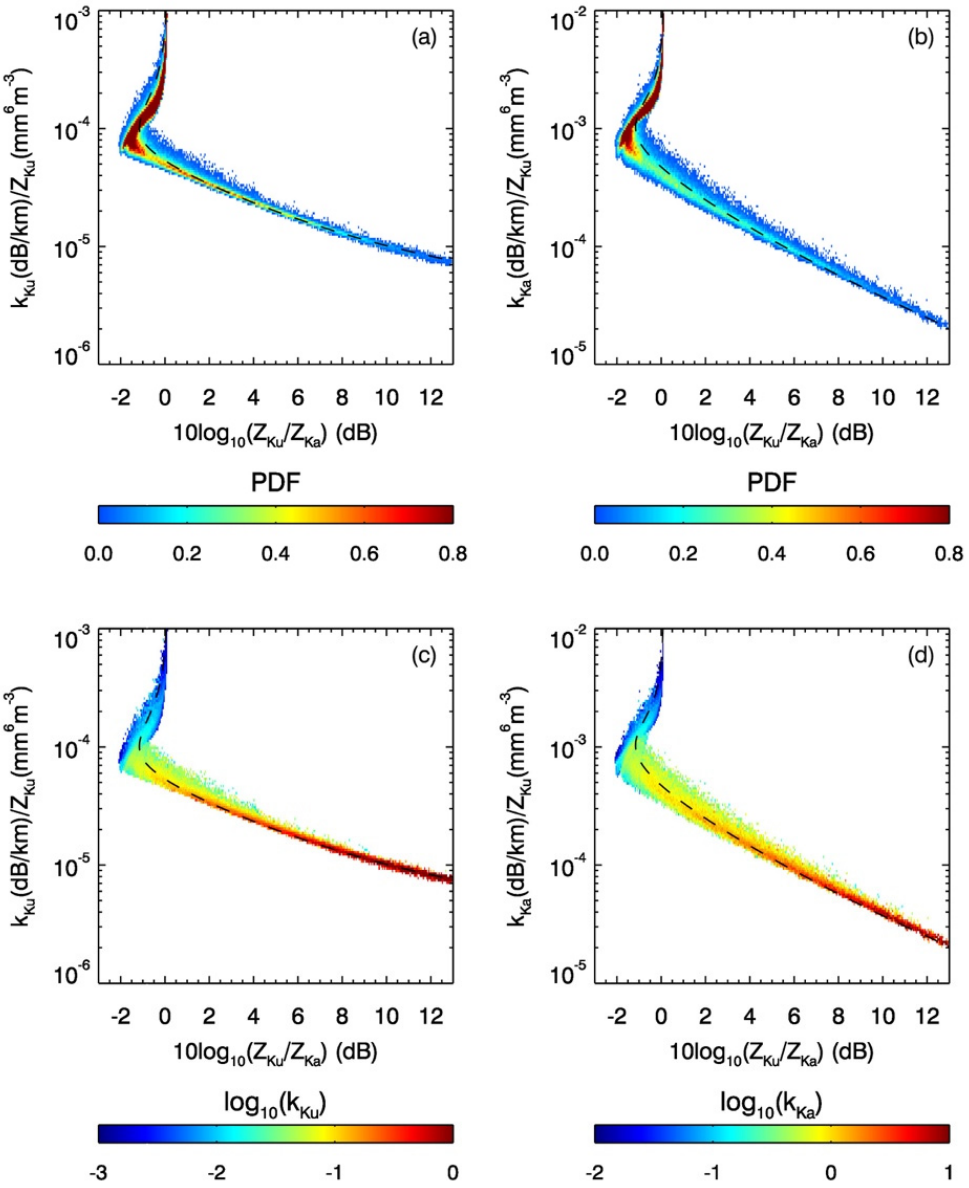

Figure 8. PDFs of the data obtained from the measured DSD. (**a**) Relationship between k_{Ku}/Z_{Ku} and DFR. (**b**) Same as (**a**) but for k_{Ka}/Z_{Ku}–DFR. Also shown are the images of the averaged k_{Ku} and k_{Ka} in the planes of the k_{Ku}/Z_{Ku}–DFR (**c**) and k_{Ka}/Z_{Ku}–DFR (**d**), respectively. The computational results from the gamma DSD model with $\mu = 3$ (black dashed lines) are provided.

6. Summary and Conclusions

With the use of 213,465 one-minute-integration-time DSD measurements collected during the field campaigns at three geographically different sites and also with use of the gamma DSD model, the statistical interrelationships among the DSD bulk parameters of R, D_m and N_w are studied. According to the definition of N_w, there exists an analytical relationship between LWC, D_m and N_w. To explore similar relationships among the variables R, D_m and N_w, a power-law fit is applied to the data of R/N_w and D_m computed from the gamma DSD model with various μ values. It is found that the model-simulated R/N_w vs. D_m results are nearly independent of μ. Furthermore, they conform well with those derived from the DSD data. Like the model results, the measured DSD show very little spread, implying a very strong relationship between R, D_m and N_w. This leads to the conclusion that R can be determined with high accuracy if D_m and N_w are known. A similar conclusion holds for D_m and N_w, i.e., D_m can be derived from R and N_w, and N_w can be obtained from R and D_m with a high

degree of accuracy Comparisons among the estimates of R, D_m and N_w from the fitting equations to their respective true values demonstrate that nearly perfect correlations exist between the estimates and the true values with negligibly small rms errors.

Although R, D_m and N_w are closely interrelated and one parameter is accurately expressed as a function of the other two parameters as in Equations (16)–(18), i.e., three-parameter relations, the constraints among these variables sometimes need to be loosened to be consistent with the limited number of radar measurements. In many situations where the radar equations are under constrained, the three-parameter relations of R, D_m and N_w need to be replaced by two-parameter relations. It is then useful to investigate statistical relationships between R and D_m, N_w and R, and N_w and D_m as in previous studies [18,26,34]. It is found from this study that R and D_m are moderately correlated while N_w and D_m are moderately negatively correlated. N_w and R, however, are uncorrelated. Because of the generally weak correlations in these two-parameter relationships (R–D_m, N_w–R and N_w–D_m), the data spread is relatively large, resulting in large errors in the estimates. Large variability in the two-parameter relationships is caused by not taking into account variations in the third parameter. For example, variability of the R–D_m relation is the result of variation in N_w. To improve retrieval accuracy by lessening the uncertainties of the two-parameter relations, additional constraints are sometimes adopted, such as the GPM DPR that is based on adjustable R–D_m relation with which an adjustable parameter ε is fixed throughout the range gates of one profile but varies from profile to profile. It is worthwhile mentioning that adjusting ε in the R–D_m relation would be equivalent to an adjustment of N_w if the exponent of the R–D_m relation is set to the value of 4.706 as derived from the fixed-μ gamma DSD. However, the exponents of the R–D_m relation implemented in the GPM DPR algorithm are 6.131 and 5.420 for stratiform and convective rain, respectively, leading to change of N_w with D_m in a way by which N_w is proportional to $D_m^{-1.425}$ and $D_m^{-0.714}$ for stratiform and convective storms, respectively. Use of adjustable R–D_m relation for the DSD profiling retrieval originates from the concept of the 'two-scale' DSD model proposed by Kozu and Nakamura [35] that allows one DSD parameter being constant over a certain space or time domains while another DSD parameter changes dynamically. Employing two-year DSD data in testing rain retrieval, they found that constant drop number concentration N_T (the 0th moment of DSD) or constant N_0 of (9) seems to be reasonable. Based on our analysis of the gamma DSD-based regression among R, D_m and N_w, constant N_w of the 'two-scale' model is perhaps another practical choice. Further study is required to examine the sensitivity of the DSD estimates to the choice of constant DSD parameters or different exponents of the R–D_m relation toward understanding and improvement of the GPM DPR performance in estimates of DSD parameters.

Our study has also been extended to look into the statistical characterization of relationships between the DSD parameters on one hand and the Ku- and Ka-band dual-frequency radar parameters on the other. To account for rain attenuation, specific attenuations are included. D_m is directly related to DFR. In contrast, R and N_w, as well as k_{Ku} and k_{Ka}, depend not only on DFR but also on Z_{Ku} or Z_{Ka}. To relate them to the dual-frequency radar measurements, a Z_{Ku}-normalization factor is used so that the Z_{Ku}-normalized R, N_w, k_{Ku} and k_{Ka}, which are obtained from the measured DSD, can be expressed as a function of DFR. The theoretical computations from a fixed $\mu = 3$ gamma DSD model are compared with the DSD-simulated results. Comparisons of the results shows fairly good agreement between the model computations and DSD data. Not surprisingly, there exist double-solution regions where DFR < 0, in which two values of the estimates are detected for a given DFR. Since no independent information is available to aid in selection of the solution, the double solutions lead to ambiguities in the estimates. A few methods attempting to mitigate the double-value issues include use of the modified dual-frequency standard technique [12] and use of the R–D_m relation [9,26]. In the region with DFR > 0, a robust one-to-one relation between DFR and normalized DSD and specific attenuation parameters ensures the soundness of the retrieval. Analysis of the results also indicates that there are smaller uncertainties in the estimates of R than in the estimates of D_m and N_w as a result of the

relatively small variability in R as compared with that in D_m and N_w. In addition, the combination of Z_{Ku} and DFR leads to fairly good estimates of k_{Ku} and k_{Ka} if the DFR is positive.

Author Contributions: Methodology, L.L. and R.M.; data and analysis: T.I. and, A.T.; writing—original draft, L.L.; Writing—review & editing, R.M., T.I. and A.T. All authors have read and agreed to the published version of the manuscript.

Funding: This research was funded by NASA's Precipitation Measurement Mission (PMM) Grant NNH18ZDA001N-PMMST.

Acknowledgments: This work is supported by G.D. Skofronick-Jackson of NASA Headquarters under NASA's Precipitation Measurement Mission (PMM) Grant NNH18ZDA001N-PMMST. The authors also wish to thank the NASA PMM ground validation team for providing and processing DSD data.

Conflicts of Interest: The authors declare no conflict of interest.

References

1. Rosenfeld, D.; Ulbrich, C.W. Cloud microphysical properties, processes, and rainfall estimation opportunities. *Meteorol. Monogr.* **2003**, *30*, 237–258. [CrossRef]
2. Meneghini, R.; Kozu, T.; Kumagai, H.; Boncyk, W.C. A study of rain estimation methods from space using dual-wavelength radar measurements at near-nadir incidence over ocean. *J. Atmos. Oceanic Technol.* **1992**, *9*, 364–382. [CrossRef]
3. Meneghini, R.; Kumagai, H. Characteristics of the vertical profiles of dual-frequency, dual-polarization radar data in stratiform rain. *J. Atmos. Oceanic Technol.* **1994**, *11*, 701–711. [CrossRef]
4. Meneghini, R.; Kumagai, H.; Wang, J.; Iguchi, T.; Kozu, T. Microphysical retrievals over stratiform rain using measurements from an airborne dual-wavelength radar-radiometer. *IEEE Trans. Geosci. Remote Sens.* **1997**, *29*, 690–703.
5. Iguchi, T.; Kozu, T.; Meneghini, R.; Awaka, J.; Okamoto, K. Rain-profiling algorithm for the TRMM precipitation radar. *J. Appl. Meteorol.* **2000**, *39*, 2038–2052. [CrossRef]
6. Iguchi, T.; Kozu, T.; Kwiatkowski, J.; Meneghini, R.; Awaka, J.; Okamoto, K.I. Uncertainties in the rain profiling algorithm for the TRMM Precipitation Radar. *J. Meteorol. Soc. Jpn.* **2009**, *87A*, 1–30. [CrossRef]
7. Seto, S.; Iguchi, T.; Oki, T. The basic performance of a precipitation retrieval algorithm for the Global Precipitation Measurement mission's single/dual frequency radar measurements. *IEEE Trans. Geosci. Remote Sens.* **2013**, *51*, 5239–5251. [CrossRef]
8. Liao, L.; Meneghini, R.; Tokay, A. Uncertainties of GPM DPR rain estimates caused by DSD parameterizations. *J. Appl. Meteorol. Climatol.* **2014**, *53*, 2524–2537. [CrossRef]
9. Seto, S.; Iguchi, T. Intercomparison of attenuation correction methods for the GPM dual-frequency precipitation radar. *J. Atmos. Oceanic Technol.* **2015**, *32*, 915–926. [CrossRef]
10. Grecu, M.; Olson, W.S.; Munchak, S.J.; Ringerud, S.; Liao, L.; Haddad, Z.; Kelley, B.L.; McLaughlin, S.F. The GPM combined algorithm. *J. Atmos. Oceanic Technol.* **2016**, *33*, 2225–2245. [CrossRef]
11. Liao, L.; Meneghini, R. Physical Evaluation of GPM DPR Single- and Dual-Wavelength Algorithms. *J. Atmos. Ocean. Technol.* **2019**, *36*, 883–902. [CrossRef]
12. Liao, L.; Meneghini, R. A Modified Dual-Wavelength Technique for Ku- and Ka-band Radar Rain Retrieval. *J. Appl. Meteorol. Climatol.* **2019**, *58*, 3–18. [CrossRef]
13. Tokay, A.; Short, D.A. Evidence from tropical raindrop spectra of the origin of rain from stratiform versus convective clouds. *J. Appl. Meteorol.* **1996**, *35*, 355–371. [CrossRef]
14. Kozu, T.; Reddy, K.K.; Mori, S.; Thurai, M.; Ong, J.T.; Rao, D.N. Seasonal and diurnal variations of raindrop size distribution in Asian monsoon region. *J. Meteorol. Soc. Jpn.* **2006**, *84A*, 195–209. [CrossRef]
15. Krishna, U.V.M.; Reddy, K.K.; Seela, B.K.; Shirooka, R.; Lin, P.-L.; Pan, C.-J. Raindrop size distribution of easterly and westerly monsoon precipitation observed over Palau islands in the Western Pacific Ocean. *Atmos. Res.* **2016**, *174–175*, 41–51. [CrossRef]
16. Gorgucci, E.; Scarchilli, G.; Chandrasekar, V.; Bringi, V. Measurement of mean raindrop shape from polarimetric radar observations. *J. Atmos. Sci.* **2000**, *57*, 3406–3413. [CrossRef]
17. Gorgucci, E.; Scarchilli, G.; Chandrasekar, V.; Bringi, V. Estimation of raindrop size distribution parameters from polarimetric radar measurements. *J. Atmos. Sci.* **2002**, *59*, 2373–2384. [CrossRef]

18. Testud, J.; Oury, S.; Black, R.A.; Amayenc, P.; Dou, X.K. The concept of "normalized" distribution to describe raindrop spectra: A tool for cloud physics and cloud remote sensing. *J. Appl. Meteorol.* **2001**, *40*, 1118–1140. [CrossRef]
19. Bringi, V.; Huang, G.; Chandrasekar, V.; Gorgucci, E. A methodology for estimating the parameters of a Gamma raindrop size distribution model from polarimetric radar data: Application to a squall-line event from the TRMM/Brazil campaign. *J. Ocean. Atmos. Technol.* **2002**, *19*, 633–645. [CrossRef]
20. Williams, C.; Bringi, V.N.; Carey, L.D.; Chandrasekar, V.; Gatlin, P.N.; Haddad, Z.S.; Tanelli, S. Describing the shape of raindrop size distributions using uncorrelated raindrop mass spectrum parameters. *J. Appl. Meteorol. Climatol.* **2014**, *53*, 1282–1296. [CrossRef]
21. Hou, A.Y.; Kakar, R.K.; Neeck, S.; Azarbarzin, A.A.; Kummerow, C.D.; Kojima, M.; Oki, R.; Nakamura, K.; Iguchi, T. The global precipitation measurement mission. *Bull. Am. Meteorol. Soc.* **2014**, *95*, 701–722. [CrossRef]
22. Skofronick-Jackson, G.; Kirschbaum, D.; Petersen, W.; Huffman, G.; Kidd, C.; Stocker, E.; Kakar, R. The Global Precipitation Measurement (GPM) mission's scientific achievements and societal contributions: Reviewing four years of advanced rain and snow observations. *Quart. J. Roy. Meteorol. Soc.* **2018**, *144*, 27–48. [CrossRef] [PubMed]
23. Tokay, A.; Wolff, D.B.; Petersen, W.A. Evaluation of the new version of laser-optical disdrometer, OTT Parsivel^2. *J. Atmos. Oceanic Technol.* **2014**, *31*, 1276–1288. [CrossRef]
24. Liao, L.; Meneghini, R.; Tokay, A.; Bliven, L.F. Retrieval of snow properties for Ku- and Ka-band dual-frequency radar. *J. Appl. Meteorol. Climatol.* **2016**, *55*, 1845–1858. [CrossRef]
25. Lhermitte, R. Observation of rain at vertical incidence with a 94 GHz Doppler radar: An insight on Mie scattering. *Geophys. Res. Lett.* **1988**, *15*, 1125–1128. [CrossRef]
26. Seto, S.; Shimozuma, T.; Iguchi, T.; Kozu, T. Spatial and temporal variations of mass-weighted mean diameter estimated by GPM/DPR. In Proceedings of the IEEE International Geoscience and Remote Sensing Symposium (IGARSS), Beijing, China, 10–15 July 2016; pp. 3938–3940. [CrossRef]
27. Thurai, M.; Huang, G.J.; Bringi, V.N.; Randeu, W.L.; Schönhuber, M. Drop shapes, model comparisons, and calculations of polarimetric radar parameters in rain. *J. Atmos Oceanic Technol.* **2007**, *24*, 1019–1032. [CrossRef]
28. Mishchenko, M.I.; Travis, L.D. Capabilities and limitations of a current FORTRAN implementation of the T-matrix method for randomly oriented, rotation symmetric scatterers. *J. Quan. Spec. Rad. Transf.* **1998**, *60*, 309–324. [CrossRef]
29. Hitschfeld, W.; Bordan, J. Errors inherent in the radar measurement of rainfall at attenuating wavelengths. *J. Meteorol.* **1954**, *11*, 58–67. [CrossRef]
30. Iguchi, T.; Meneghini, R. Intercomparison of single-frequency methods for retrieving a vertical rain profile from airborne or spaceborne radar data. *J. Atmos. Oceanic Technol.* **1994**, *11*, 1507–1516. [CrossRef]
31. Liao, L.; Meneghini, R. A Study on the feasibility of dual-wavelength radar for identification of hydrometeor phases. *J. Appl. Meteorol. Clim.* **2011**, *50*, 449–456. [CrossRef]
32. Le, M.; Chandrasekar, V. Hydrometeor profile characterization method for dual-frequency precipitation radar onboard the GPM. *IEEE Trans. Geosci. Remote Sens.* **2013**, *51*, 3648–3658. [CrossRef]
33. Iguchi, T.; Seto, S.; Meneghini, R.; Yoshida, N.; Awaka, J.; Le, M.; Chandrasekar, V.; Brodzik, S.; Kubota, T. GPM/DPR Level-2 Algoirthm Theoretical Basis Document. Available online: https://pps.gsfc.nasa.gov/Documents/ATBD_DPR_202006_with_Appendix_a.pdf (accessed on 1 June 2020).
34. Bringi, V.N.; Chandrasekar, V.; Hubbert, J.; Gorgucci, E.; Randeu, W.L.; Schoenhuber, M. Raindrop size distribution in different climatic regimes from disdrometer and dual-polarized radar analysis. *J. Atmos. Sci.* **2003**, *60*, 354–365. [CrossRef]
35. Kozu, T.; Nakamura, K. Rainfall parameter estimation from dual-radar measurements combining reflectivity profile and path-integrated attenuation. *J. Atmos. Oceanic Technol.* **1991**, *8*, 259–270. [CrossRef]